Lock-in amplifier-based rotating-analyzer spectroscopic ellipsometer with micro-controlled angular frequency

J.M. Flores-Camacho*, O.F. Núñez-Olvera, G. Rodríguez-Pedroza, A. Lastras Martínez, and L.F. Lastras-Martínez**
*Instituto de Investigación en Comunicación Óptica, Universidad Autónoma de San Luis Potosí,
Álvaro Obregón 64, 78000 San Luis Potosí, S.L.P., Mexico*

We report on the development of a full operational rotating analyzer spectroscopic ellipsometer. This instrument employs a phase-sensitive amplifier to process the optical signal as an alternative to Fast Fourier Transform analysis. We describe electronic hardware designed to stabilize the rotation frequency of the analyzer prism as well as to drive the device for the positioning of the polarizer prism azimuth. The ellipsometer allows for dielectric function measurement in the energy range from 1.7-5.5 eV, in both ambient air and Ultra High Vacuum (UHV). UHV measurements can be carried out at a temperature as low as 150 K. To evaluate the ellipsometer performance we present results of the determination of the complex dielectric function of a number of semiconductors, namely, GaSb, GaAs, InGaAs, CdTe and CdHgTe.

Keywords: Ellipsometers; control systems; dielectric function; optical properties of thin films

Se describen el diseño, la construcción y la operación de un elipsómetro espectroscópico de analizador rotante. El instrumento hace uso de un amplificador sensible a la fase para procesar la señal óptica; esto como una alternativa al análisis de la misma por la técnica de Trasformada Rápida de Fourier. Cuenta con dispositivos electrónicos diseñados para controlar la frecuencia de rotación del prisma analizador, así como para posicionar el ángulo azimutal del prisma polarizador. El elipsómetro permite la medición de la función dieléctrica en el rango de energías desde 1.7 eV hasta 5.5 eV, tanto en aire como en condiciones de Ultra Alto Vacío (UHV). En UHV es posible realizar mediciones a temperaturas tan bajas como 150 K. Para evaluar la operación del elipsómetro, se presentan resultados de la medición de la función dieléctrica de un número de semiconductores, en forma específica, de GaSb, GaAs, InGaAs, CdTe y CdHgTe.

Descriptores: Elipsómetros; sistemas de control; función dieléctrica; propiedades ópticas de películas delgadas.

PACS: 07.60.Fs, 07,05.Dz; 78.20.-e; 78.66.-w

1. Introduction

The precise determination of the complex dielectric function [1] of a semiconductor, and thus of its optical properties [2], is of fundamental importance for both basic and applied points of view. First of all, this determination is essential in order to understand the physics underlying the optical response of semiconductors [3–5]. Knowledge of the dielectric function of a semiconductor, for instance, allows for the determination of its critical point energies, which played a prominent role in the understanding of the electronic structure of semiconductors. The experimental determination of the dielectric function plays a prominent role as well in the development of new materials and devices. In this regard, among the information we may obtain from the dielectric function, we include epilayer thickness and composition in semiconductor heterostructures [6,7], epilayer strain induced by lattice mismatch [8, 9], and quantum confinement effects in low-dimensional structures [10–12].

Spectroscopic ellipsometry (SE) is a well-known non-destructive technique for the experimental determination of the complex dielectric response of semiconductors [1, 13]. Photometric-dynamic ellipsometers, which rely on the time-modulation of the polarization of light, have many advantages with respect to those of null design; they may, for instance, operate with relatively weak light sources and can be instrumentally automated [6, 14, 15]. Ellipsometry provides two parameters in a single measurement, thus allowing for the simultaneous determination of both the real and imaginary parts of the dielectric function with no need for further Kramers-Kronig analysis. SE presents advantages over single-parameter techniques, such as spectroscopic reflectivity, as it allows for the possibility of numerically removing surface overlayers and roughness effects [4].

Ellipsometry is based on the fact that linearly-polarized light incident on a medium at an oblique angle is in general reflected with an elliptic polarization [1]. The change in light polarization upon reflection carries information of the optical properties of the medium under consideration [4]. Two kinds of automatic photometric ellipsometers have been developed:

1) instruments employing a photoelastic modulator to switch between parallel and perpendicular polarizations of the incident, light which are characterized by their high speed [16], and

2) rotating-analyzer ellipsometers (RAE), which offer both a simpler design and data interpretation. RAEs are the preferred choice when both accuracy and precision are required [14, 17].

In this paper, we report on the development of a spectroscopic ellipsometer of the rotating-analyzer type. This instrument is based on the use of a phase-sensitive amplifier for the processing of the optical signal as an alternative to Fast Fourier Transform analysis [14]. This results in a somewhat simpler procedure for the determination of the ellipsometric parameters [14].

We further describe electronic hardware designed for both the determination of the optical plane of incidence, and the frequency stabilization of the rotating analyzer prism. As is well known, an accurate measurement of the dielectric function calls for an accurate determination of the optical plane of incidence. To enhance the signal-to-noise ratio, on the other hand, it is crucial to stabilize the analyzer rotation frequency.

The rest of the paper is organized as follows. In Sec. 2 we describe the optical arrangement and instrumental implementation of the ellipsometer. Alignment calibration and experimental data acquisition are described in Sec. 3. In Sec. 4, we present measurements of dielectric functions for a number of semiconductors in order to evaluate the operation of the instrument. Finally, conclusions are given in Sec. 5.

2. Instrument description

2.1. Optical setup

The configuration of the ellipsometer described here is of the polarizer-sample-analyzer (PSA) type. In Fig. 1 we show a schematic diagram of this configuration. Monochromatic light is passed through a linear polarizer with an azimuth angle P and focused on a sample surface. After reflection, light is passed through a rotating linear polarizer and finally is detected by a photomultiplier tube. This set up produces a time-dependent signal at the output of the photodetector.

Two light sources are employed in the ellipsometer set up, a 75 W Xe short-arc lamp suitable for measurements in the energy range from 2.7 to 5.5 eV and a 150 W tungsten lamp for the $1.7 - 3.0$ eV energy range. By using a tungsten lamp in the near IR range we avoid the energy range of the Xe lamp that is dominated by line spectra [18]. Both light sources are located in the same housing. Lamps are selected by a simple mechanism and only a small realignment is necessary upon shifting them.

The light beam exiting from the source lamp is focused by means of two $f/6$ spherical mirrors at the entrance slit of a $0.5 -$ meter focal length monochromator (Jobin-Yvon-Spex, model HR-460, $f/5.3$). Two diffraction gratings (1200 and 600 lines/mm) allows for photon energy scanning from 1.7 to 5.5 eV. Light exiting the monochromator is collimated with a $4''$ focal length $f/2$ mirror. Two corrected Rochon quartz prisms (Optics for Research, model PUR-10-2-X-Z with less than 10 sec ordinary ray beam deviation) were used as polarizer and analyzer devices. Light reflected by the sample impinges on the analyzer prism wedge that linearly polarizes the elliptic beam. The second wedge works as a depolarizer, thus a time dependent modulated signal reaches the detector [19]. The extraordinary ray beam at the output of the polarizer is blocked by an iris diaphragm that is also useful in reducing the light spot to fit the sample surface area (less than 1×1 cm^2).

Upon reflection on the sample surface, light becomes in general elliptically polarized due to the different phase shift between s and p polarizations. It is the aim of ellipsometry to determine the parameters (azimuth and ellipticity) of the polarization ellipse. This is done through the Fourier analysis of the time-dependent photodetector output signal. Details of this analysis are discussed in the next section.

The azimuth angle of the polarizer was set to $P = 30°$ [14]. We used an angle of incidence of $67°$. This angle is close to Brewster's angle for most semiconductors in the wavelength range of interest, and maximizes the difference in phase shift that the s and p beam components experience upon reflexion.

The instrument allows for measurements in both ambient air and Ultra-High-Vacuum (UHV). In the latter case, the sample is placed inside UHV chamber with a base pressure in the low 10^{-10} Torr range. Light is introduced/extracted through strain-free fused quartz optical ports (Fig. 2). The sample manipulator permits heating up to 1200K, thus allowing for the removal of either the surface oxide or the protective layer arsenic that is sometimes deposited to avoid oxidation. The sample holder allows as well for sample cooling down to 150K.

Light is detected by means of a Hamamatsu R1464 end-on photomultiplier with a GaAs photocathode. This photomultiplier was selected because of its high sensitivity and relatively low polarization dependence [14].
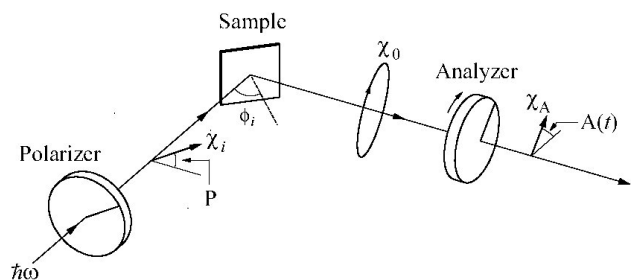

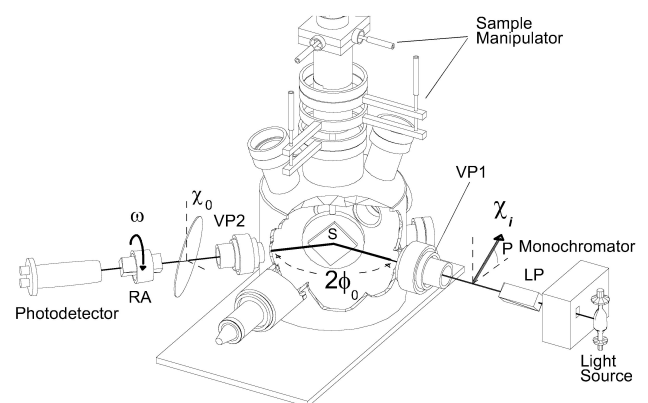FIGURE 1. Schematics of the PSA ellipsometer with the angle convention used in this work.

FIGURE 2. Basic set up of the rotating-analyzer ellipsometer adapted to a UHV chamber. S is the sample, ϕ_0 is the angle of incidence, ω is the angular frequency of the analyzer and [VP1], [VP2] are the strain-free optical ports. RA and LP stand for rotating analizer and linear polarizer prisms, respectively.

2.2. Optical analysis

Light polarization is conveniently specified in terms of the complex variable χ defined as

$$\chi = \frac{E_s}{E_p} \tag{1}$$

where E_s and E_p are, respectively, the perpendicular and parallel electric field complex components of the electromagnetic wave (Fig. 1).

In terms of the polarizations of the reflected wave, χ_0, and the wave exiting the analyzer χ_A, where

$$A = \omega t + A_0 \tag{2}$$

is the angle of the analyzer prism, the light intensity reaching the photodetector may be obtained from the squared magnitude of the projection of the incoming polarization on the analyzer orientation

$$I = \frac{\left| (E_{Ax}^* \ \ E_{Ay}^*) \begin{pmatrix} E_{0x} \\ E_{0y} \end{pmatrix} \right|^2}{|\vec{E}_A|^2 |\vec{E}_0|^2}. \tag{3}$$

From Eqs. (1) and (3) we may write

$$I(t) = I_0 \frac{\chi_0 \chi_0^* \chi_A \chi_A^* + \chi_0 \chi_A^* + \chi_A \chi_0^* + 1}{\chi_0 \chi_0^* \chi_A \chi_A^* + \chi_0 \chi_0^* + \chi_A \chi_A^* + 1}, \tag{4}$$

where I_0 is the light intensity reflected by the sample.

If the reference of the analyzer is arbitrarily chosen as in Eq.(2), the polarization state at the output of the analyzer is

$$\chi_A = \frac{\tan A + \chi_{A0}}{1 - \chi_{A0} \tan A}, \tag{5}$$

where χ_{A0} is the polarization state at $A(t = 0)$. However, this expression can be simplified by assuming a time reference so that $A_0 = 0$ [20], as $\chi_A = \tan A$ (see Fig. 1). Accordingly, we may write Eq. (4) in the form

$$I(t) = \frac{I_0}{2}(1 + \alpha \cos 2A + \beta \sin 2A) \tag{6}$$

where α and β are the normalized Fourier coefficients given by

$$\alpha = \frac{1 - |\chi_0|^2}{1 + |\chi_0|^2} \tag{7}$$

and

$$\beta = \frac{2Re(\chi_0)}{1 + |\chi_0|^2} \tag{8}$$

From Eqs. (7) and (8) the polarization of the light reflected by the sample is given by

$$\chi_0 = \frac{1}{1 + \alpha} \left[\beta \pm i(1 - \alpha^2 - \beta^2)^{\frac{1}{2}} \right], \tag{9}$$

where the $\pm$ sign indicates that the handedness of the elliptic polarization is not determined, *i.e.*, both polarizations χ_0 and χ_0^* lead to the same α and β Fourier coefficients [20].

Taking into account that the state of polarization of the incident light for a PSA system is given by $\chi_i = \tan P$, the complex reflectance ratio $\rho = \chi_i/\chi_0$ [21, 22] is

$$\rho = \frac{(1 + \alpha) \tan P}{\beta \pm i(1 - \alpha^2 - \beta^2)^{\frac{1}{2}}}. \tag{10}$$

Eq.(10) is valid only for ideal polarizers; consequently, it is applicable when precision rather than accuracy is of primary importance, otherwise the effects of the optical activity of both polarizer and analyzer prisms must be taken into account [23].

The sample complex dielectric response is given as a function of the ratio ρ as [1]

$$\varepsilon = \sin^2 \phi_i \left[1 + \tan^2 \phi_i \left(\frac{1 - \rho}{1 + \rho} \right)^2 \right], \tag{11}$$

where ϕ_i is the angle of incidence.

3. Instrumental Implementation

3.1. Mechanical system

An accurate control of the polarizer angular position of the polarizer prism is essential for the determination of the optical plane of incidence. To achieve this control, the polarizing prism is mechanically coupled to a stepping motor with a $10 : 1$ gear ratio. This ratio leads to a resolution of the polarizer angular position of $\sim 0.09^o$ /step. The stepping motor is controlled by the ellipsometer computer.

The sample-holders for both ambient air and UHV operation allow for a precise sample alignment, *i.e*, $x - y - z$ motions, quantification of the angle of incidence and optical plane correction. The sample holder for ambient air is a home-made plate similar to the one described in Ref. 24. For the UHV chamber the manipulator is equipped with a heater, an N_L cooling system and a K-type thermocouple.

The analyzer prism rotor is one of the critical components of the ellipsometer. It must allow for prism rotation, both vibration and precession-free, at a mechanical frequency of around 45 Hz. In our case, the analyzer prism ([A] Fig. 3) is held in place inside a hollow steel cylinder [D] with the help of six adjusting screws [E]. These screws, three at each end of the prism cylinder, permit the prism to be aligned concentrically with the rotation axis. The analyzer prism is driven by a D.C. electric motor [M] with a 3300 rev/min maximum speed. The motor shaft is coupled to the prism rotor with the help of a transmission band [B] and a pulley [C]. The rotor is mounted on two sealed bearings [G] fastened to the rotor housing [F]. The reference signal for the phase-sensitive amplifier is provided by an arrangement consisting of an emitter-photodetector pair [I] and a rotating half-plate blade [H]. The motor rotation frequency is controlled through a micro-encoder [J] as detailed in the next subsection.
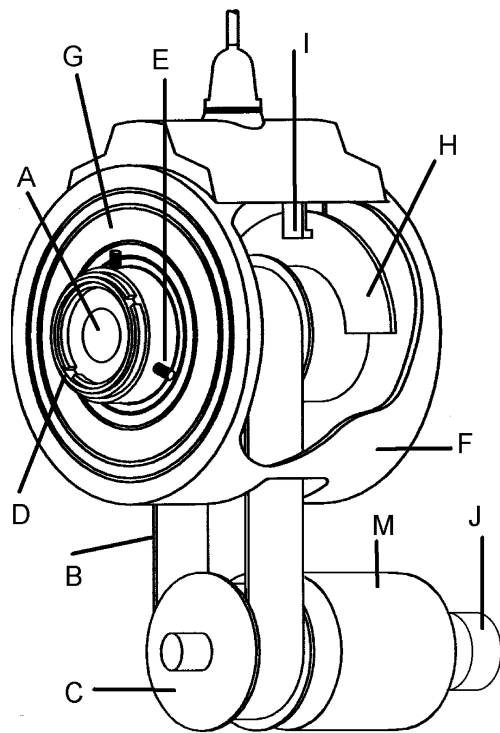
FIGURE 3. Mechanical assembly for the rotating analyzer of the ellipsometer. The analyzer prism [A] is mechanically coupled to the D.C. electric motor [M] by means of a transmission band [B] and a pulley [C]. The prism is held inside a cylindrical steel carrier [D] with three screws [E] fastened to a concentric exterior cylinder. This system is held in its housing [F] by two sealed bearings [G]. A half plate blade [H], passing between the emitter and the detector of the opto-pair [I] provides the lock-in amplifier reference signal. The motor velocity is measured and controlled through a micro-encoder [J].

3.2. Angular control of the polarizer

In order to control the angular position of the polarizer prism, we have used a two-winding stepping motor. The electronic circuit of the stepping motor comprises control and power stages as shown in Fig. 4. The control stage is configured by means of the integrated circuit (IC) L297 [25]. This IC generates the byte sequence to move the motor according to the input signals: $\overline{\text{CLOCK}}$ (clock), $\overline{\text{ENABLE}}$ (enable), CW/$\overline{\text{CCW}}$ (direction) and HALF/$\overline{\text{FULL}}$ (mode). These control signals are supplied by the PC through the data lines $D0 - D3$ of the parallel port. $\overline{\text{ENABLE}}$ turns on and off the output signals of the L297, $\overline{\text{CLOCK}}$ controls the speed of rotation, HALF/$\overline{\text{FULL}}$ sets the mode of rotation in half on full steps, and CW/$\overline{\text{CCW}}$ the direction of rotation, clockwise or counterclockwise.

The output signals of the L297 are connected to the power stage, designed on the basis of the H-bridge L298N [25]. The windings of the motor are connected to pins 2, 3, 13, and 14 in the L298N bridge. We have also connected eight fast diodes $(2\text{A}, \text{time response} < 200\text{ns})$ to protect the L298N IC as is it shown in Fig. 4.
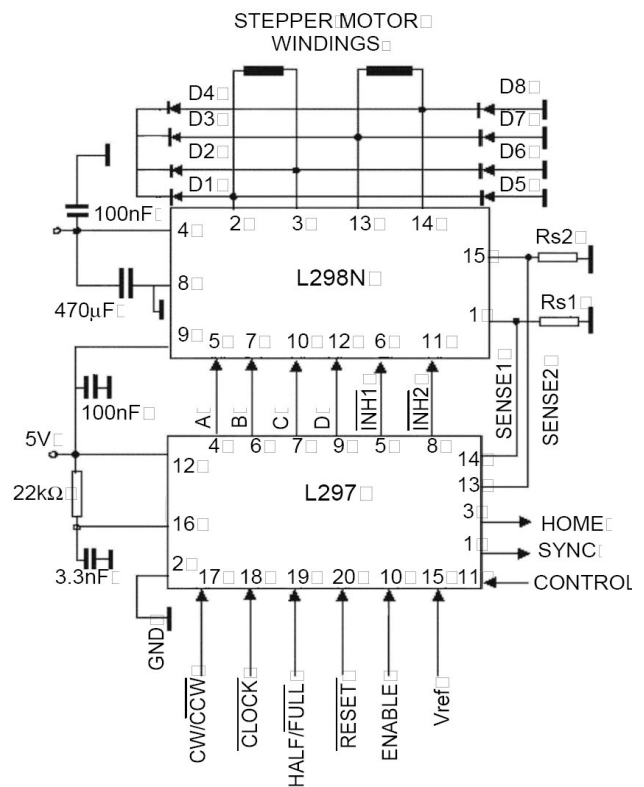

FIGURE 4. Electronic diagram of the stepper motor control. The control is formed by two parts: a control (L297) and a power (L298N) stages. We have used the values: $V_{\text{ref}} = 1.8$ V and $R_{\text{s}1} = R_{\text{s}2} = 0.3 \ \Omega$.

3.3. Speed control of the analyzer

In order to preserve calibration constants throughout the data acquisition period, the analyzer frequency must be kept stable; otherwise, it is known that frequency fluctuations lead to significant errors that cause a phase shift in the modulated signal [14], thus reducing the correlation between consecutive experimental points.

The analyzer prism is driven by a DC motor that is frequency-stabilized by a $LM629$ precision DC motor controller. The $LM629$ controller is configured by

1) a host I/O block (IOB),

2) a trapezoidal velocity profile generator block (TGB),

3) a feedback position block (FB) and

4) a digital PID filter (PID).

The IOB receives commands and motion parameters from the PC via the data lines D0-D7. With this information the TGB calculates the required trajectory. The motor position is detected by means of an optical incremental micro-encoder (MES-20-200P of MTL) with a resolution of 200 pulses per revolution, coupled to the motor shaft (see Fig. 3[J]). The A and B signals of the encoder are the input signals for the FB and provides feedback for closing the position servo loop by

means of the quadrature signal method. The $LM629$ substracts the actual position (FB position) from the desired position (TGB position) and the resulting error is processed by the signal PID filter to drive the motor to the desired position. The PID generates, according to error signal and control parameters, pulse width modulation (PWM) and rotating direction signals. These signals drive the power supplied to the motor through the H-bridge $LMD18200T$ [26].

The speed control system is mounted on two electric cards:

a) a holding control stage which is inserted into a ISA PC slot and

b) a power stage, as is shown in Fig. 5 and Fig. 6, respectively.

The interconnection between both cards is opto-coupled in order to isolate the PC from the motor power supply.

FIGURE 6. Power board diagram of the speed control of the rotating analyzer. The LMD18200 H-bridge receives the control signals DIR and MAG from the LM629 and sends the controlled voltage to the DC motor through its outputs 1 and 2.

An 8-bit magnitude comparator $74LS688$ is used as address decoder in the control stage [27]. When the address—selected by the dip switch SV1—is sent by the PC, the $74LS688$, enables the $LM629$ to receive and send data or commands.

3.4. Light detection and signal processing

We employed a photomultiplier tube (PMT) for light detection. The high voltage bias required by the photomultiplier is provided by a Kepco Operational Power Supply, model OPS 2000B with a 2.0 MΩ internal feedback resistance. The power supply is driven by a Keithley programmable current source model 220, controlled by the PC via the IEEE port. The PMT housing allows for PMT cooling to temperatures down to $-20°$C. The PMT DC output voltage is kept constant along the entire wavelength scan by varying the PMT bias through the programmable current source.

The PMT output is fed to an operational amplifier in low-pass filter configuration [14, 28]. Two selectable 10kΩ and 25kΩ feedback resistors allow for flat amplifier response (3dB) for frequencies up to 340Hz and 135Hz, respectively. The operational amplifier DC and AC outputs are measured with the help of a Keithley 2002 voltmeter and a $SR530$ Stanford Research lock-in amplifier, respectively. We have chosen a synchronous detection technique to determine the AC signal amplitude due to its band-pass filtering capability at the reference frequency. This frequency is provided by an optical encoder synchronously rotating with the analyzer prism.
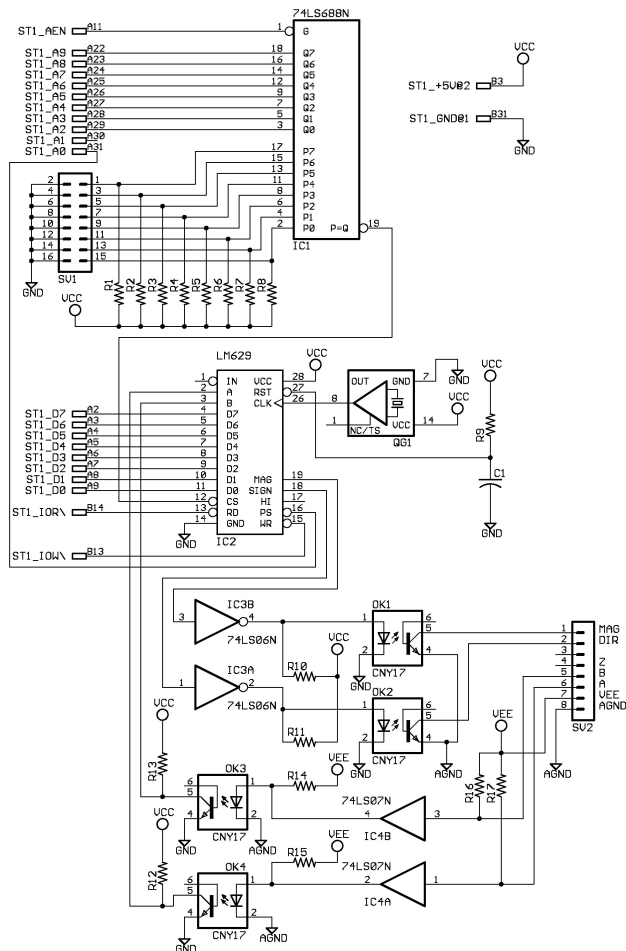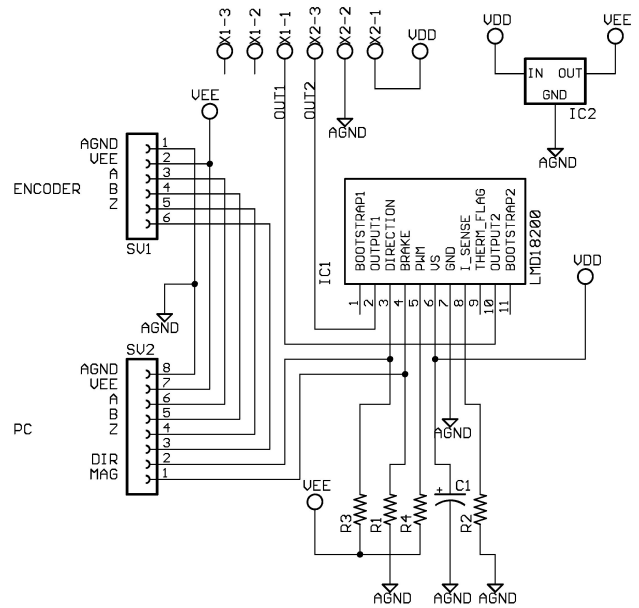

FIGURE 5. Electronic diagram of the speed control of the DC motor. The system comprises two parts: (a) the address decoder 74LS688N and (b) the microprocessor LM629. The control board is inserted in the ISA slot of the PC. The ISA signals used in the design are: $ST1\_A0 - ST1\_A9$ (address), $ST1\_AEN$ (address enable), $ST1\_D0 - ST1\_D7$ (data), $ST1\_IOR$ (Input/Output read), $ST1\_IOW$ (Input/Output write).

In terms of the output voltages provided by the light detection system, Eq. (6) may be written as [14]

$$I = k\overline{V}\left[1 + \eta a \cos 2(A + A_F) + \eta b \sin 2(A + A_F)\right], \quad (12)$$

where $\overline{V}$ is the average DC voltage, A_F is the signal phase delay due to signal-processing circuit, $1/\eta$ is the relative attenuation of the AC signal with respect to the DC component, and k is a constant of proportionality. We also have

$$a = \frac{\sqrt{2}}{\overline{V}}\nu_1 \quad (13)$$

and

$$b = \frac{\sqrt{2}}{\overline{V}}\nu_2 \quad (14)$$

where ν_1 and ν_2 are respectively, the rms phase and quadrature signal amplitudes as measured by the lock-in amplifier. We note that, so defined, a and b correspond to the normalized signal Fourier coefficients.

4. Operation

4.1. Calibration routine

As discussed in Sec. 2.2, it is convenient to choose the time reference of the rotating analyzer in order to get $A_0 = 0$. To do so, the polarizer prism is loosened from its holder and rotated to make the zero-azimuth angle position to approximately coincide with the onset of an optical encoder pulse. A more precise $A_0 = 0$ setting is used out during the calibration procedure.

The use of a synchronous detection technique to measure the signal amplitudes AC leads to a relatively simple calibration routine. The aim of this routine is to determine parameters A_F and η in Eq. (12). These parameters are necessary to obtain the complex reflectance ratio ρ from the measured a and b coefficients. The calibration procedure is based on the fact that the state of polarization of the reflected light is linear if and only if the incident light is linearly polarized either parallel or perpendicular to the plane of incidence. Calibration is initiated by manually placing the polarizer at its approximate zero-azimuth angle P_s (that will be set equal to zero). The lock-in reference phase angle is then selected so that a zero reading is obtained in one of the two signal channels. Through this zero-reading adjustment we compensate for phase angle A_F as well as for some prism alignment error that may have occurred when first attempting to establish the condition $A_0 = 0$. Next, by varying the polarizer angle around $P_s = 0$, we compute the set of residuals $r(P)$ defined by

$$r_j(P_j) = 1 - a_j^2 - b_j^2, \quad (15)$$

where j is an integer, P_j is the azimuth angle of the polarizer prism and a_j and b_j are the normalized signal Fourier coefficients. In terms of the α and β coefficients Eq. (15) is written as

$$r(P) = 1 - \frac{1}{\eta^2}(\alpha^2 + \beta^2). \quad (16)$$

We note that $r(P)$ has a minimum at $P = P^{(0)}$, where $P^{(0)}$ is the true zero azimuth angle of the polarizer. Thus, by making a power expansion of $r(P)$ around $P^{(0)}$ and by noting that $\alpha = -1$ and $\beta = 0$ at $P = P^{(0)}$, we obtain the approximate expression

$$r(P) = \left(1 - \frac{1}{\eta^2}\right) + \gamma(P - P^{(0)})^2. \quad (17)$$

Finally, by fitting Eq. 17 to the parabola [14]:

$$r(P) = c_0 + c_1 P + c_2 P^2 \quad (18)$$

we obtain

$$P^{(0)} = -\frac{c_1}{2c_2} \quad (19)$$

and

$$\eta = \left(1 - c_0 + \frac{c_1^2}{4c_2}\right)^{-\frac{1}{2}} \quad (20)$$

An example of a calibration parabola is shown in Fig. 7. Typical values for η are in the range from 1.04-1.21 while for A_F we found a value of $15°$.

The calibration procedure employed in the ellipsometer described here allows for a simple determination of the phase delay A_F as well as for a simple setting of the condition
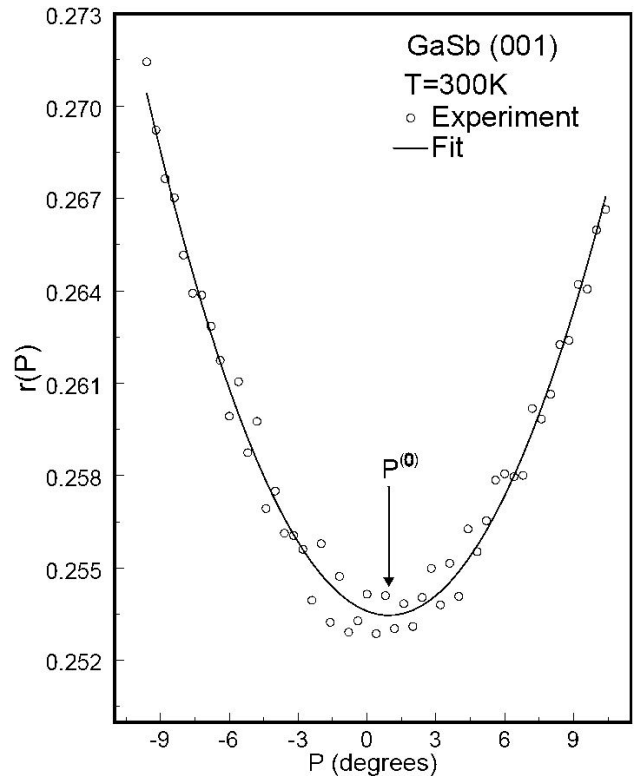

FIGURE 7. Calibration parabola used to obtain the polarizer azimuth reference angle for an n-doped GaSb (001) sample (open circles). The solid line is the best fit obtained by using Eq. (18). The fit leads to the values $\eta = 1.157$ and $P^{(0)} = 0.95°$.
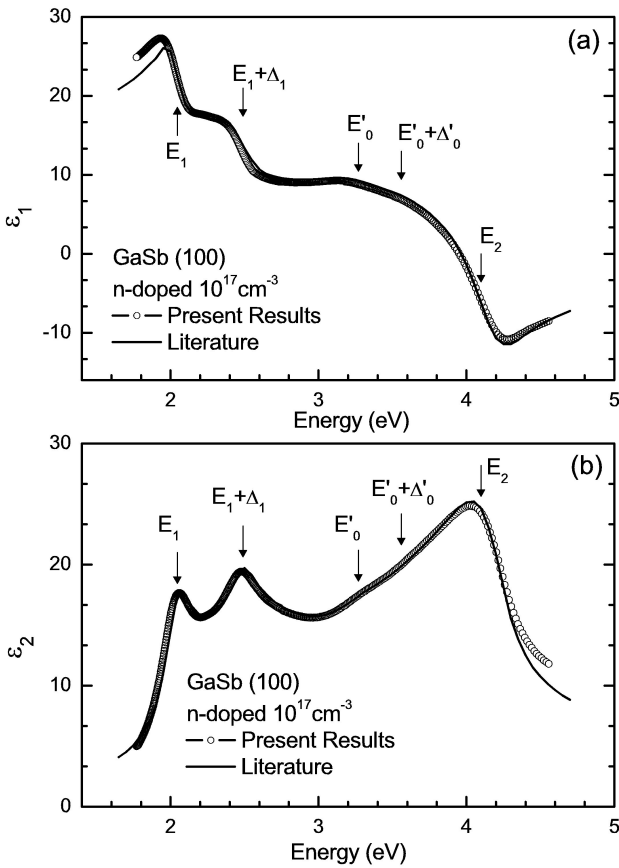
FIGURE 8. Dielectric function of n-doped (001) GaSb (open circles) compared with the results of a chemically etched surface of intrinsic GaSb (solid line) [2].

$A_0 = 0$. This leads to a somewhat simpler calibration routine than that employed by Aspnes and coworkers [14].

The calibration routine, in short, determines the actual plane of incidence given by the optics alignment and the reference analyzer prism azimuth A_0 and corrects the effects of the processing electronics on the amplitude and phase of the signal.

4.2. Data acquisition

The relation between intensity and voltage-related quantities is obtained by comparing Eqs. (6) and (12). Through this comparison we may write for parameters α and β

$$\alpha = \eta \sqrt{2} \frac{\sum_{i=1}^{N} \nu_1^{(i)} - \nu_{10}}{\sum_{i=1}^{N} \overline{V}^{(i)} - \overline{V}_0} \tag{21}$$

and

$$\beta = \eta \sqrt{2} \frac{\sum_{i=1}^{N} \nu_2^{(i)} - \nu_{20}}{\sum_{i=1}^{N} \overline{V}^{(i)} - \overline{V}_0} \tag{22}$$

where N is the number of experimental sample data at each wavelength and, ν_{10}, ν_{20} and $\overline{V}_0$ correspond to residual voltages due to environmental light, taken at the beginning of the experiment.
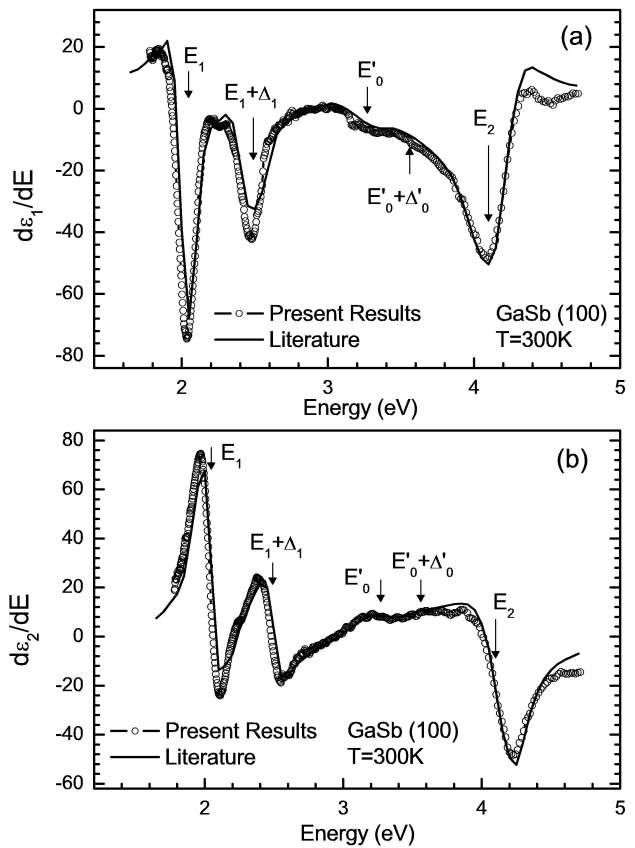

FIGURE 9. First energy-derivative of (a) real and (b) imaginary parts of the spectra shown in Fig. 8.

Discernment on the assignment of lock-in channels to α and β depends on calibration phase selection and analyzer prism direction. For the measurement of the spectra shown in Sec. 4, the ellipsometer was calibrated by using the condition $\alpha = -1$ and $\beta = 0$ of the Eq. (17) and the rotation of the analyzer prism was set as indicated in Fig. 2. Finally, the complex ratio ρ is calculated using the plus sign in Eq. (10) and then the dielectric function is obtained with Eq. (11).

5. Results

To evaluate instrument performance we have measured the dielectric function of a number of semiconductors. In Fig. 8 we show the dielectric function of a GaSb(001) cristal doped with 5×10^{17} cm^{-3} donors. The measurement was undertaken at room temperature in the energy range from 1.7 to 4.8 eV. We corrected for the surface oxide layer by using a three phase model (air/oxide/GaSb) [29] and the refractive index of the native oxide reported in the literature [30]. The real and imaginary dielectric function spectra obtained (corresponding to a 6 nm thick oxide layer) are shown with open circles in Fig. 8, along with dielectric function spectra (continuous lines) reported in the literature [2]. The values of the labeled critical points E_1 and $E_1 + \Delta_1$, 2.047 and 2.488eV, respectively, were taken from Ref. 31, while the values of E_2 and of the points of Γ symmetry E'_0 and $E'_0 + \Delta'_0$ are
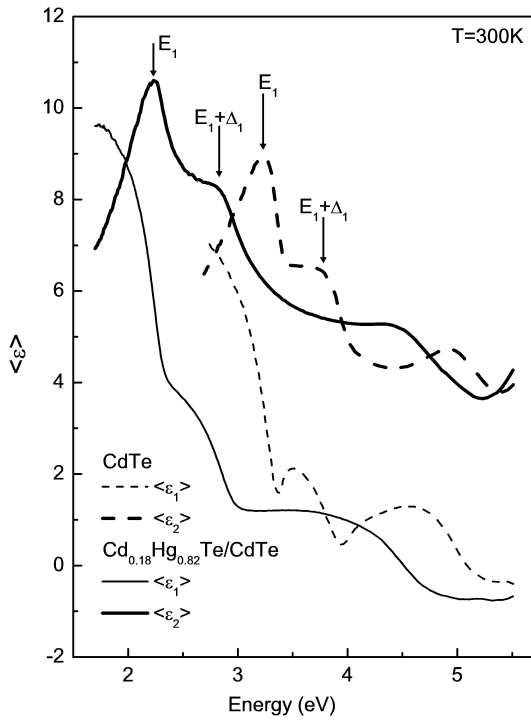
FIGURE 10. Comparison of the pseudo-dielectric functions of CdTe and a Cd$_{.18}$Hg$_{.82}$Te (1μm thick epilayer grown on CdTe).
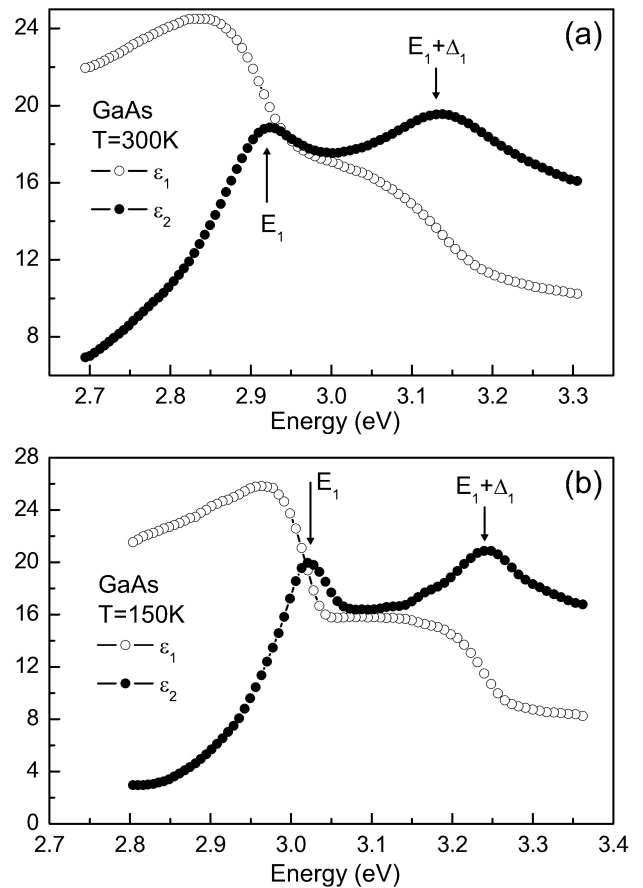

FIGURE 12. Real (open circles) and imaginary (filled circles) parts of the dielectric function of intrinsic (001)GaAs at (a) 300K and (b) 150 K around E_1 and $E_1 + \Delta_1$, measurements were carried out in ultra-high-vacuum.
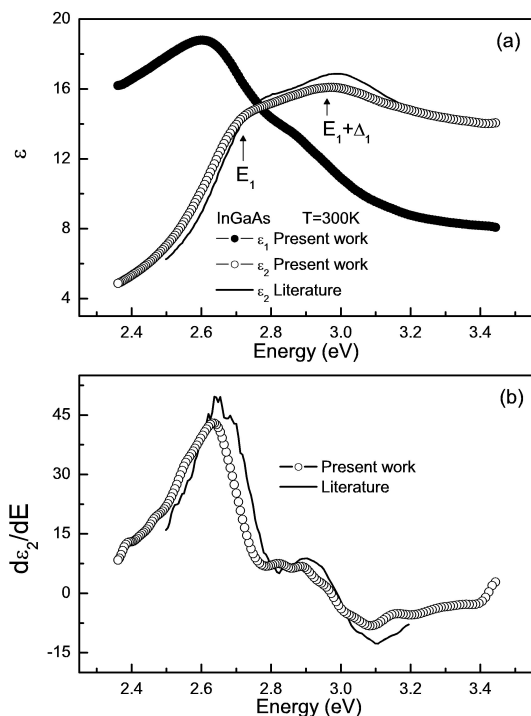

FIGURE 11.(a) The dielectric function of a 0.5 μm thick In$_{0.3}$Ga$_{0.7}$As epilayer extracted from the measured pseudo-dielectric function of an InGaAs/GaAs heterostructure grown by MBE (circles) and In$_{0.27}$Ga$_{0.73}$As from Ref. 8 (continuous line). (b) Comparison of first energy derivatives of ε_2.

from Ref. 31. We note the excellent agreement between our spectra with those previously reported.

In Fig. 9 we show the first energy-derivative of the spectra of Fig. 8. As can be seen, the signal-to-noise ratio is high enough for the derivative spectra to show a well-defined structure, allowing for a precise determination of interband transition energies.

In Fig. 10 we plot the measured pseudo-dielectric functions of CdTe (dashed lines) and Cd$_x$Hg$_{1-x}$Te (continuous lines). Measurements were performed by using a tungsten lamp for energies below 2.7 eV and a Xe lamp for higher energies. By assuming a quadratic dependence of the E$_1$ energy with CdTe composition x [32] we have determined $x \approx 0.18$. We note that the presence of a native oxide layer [33] changes the relative amplitude between E$_1$ and E$_1 + \Delta_1$ and diminishes the high energy peaks (4.5 − 5.5 eV) of $\langle \varepsilon_2 \rangle$.

As an example of the determination of the dielectric function of thin heteroepitaxial layers, in Fig. 11 we show the dielectric function of an In$_{0.3}$Ga$_{0.7}$As thin film grown by Molecular Beam Epitaxy (MBE) on a GaAs substrate. By using a three-phase model (air/epitaxial-layer/substrate) and the measured epitaxial layer thickness we could subtract the

GaAs contribution from the measured pseudodielectric function. The resulting $In_{0.3}Ga_{0.7}As$ dielectric function is shown with open circles in Fig. 12(a), along with the dielectric function of $In_{0.27}Ga_{0.73}As$ (continuous lines) reported in the literature [8]. As it can be seen, the agreement of our spectra with those of the literature is excellent.

As a final result, we would like to report on the measurement of the dielectric function of a non-doped MBE GaAs (001) epilayer, at both room temperature and at T=150K. Results are shown in Fig. 12(a) (room temperature) and Fig. 12(b) (T=150K). The measurements were carried out inside the UHV chamber. The samples were covered with an As_2 film in order for them to be transferred form the growth chamber to the ellipsometer chamber. Once inside this last chamber the As_2 film was thermally desorbed previously to measurement. The chamber pressure was kept in the lower 10^{-10} range after desorption. Notice that the energy peaks are narrowed and shifted to higher energies as the temperature decreases. Both the energy shift ($\sim 90\,$meV) and broadenings observed in our experiments are consistent with those reported in the literature [34].

Finally, by using Eqs.(5a-b) and (8b) of Ref. 23 we calculated the effect of the analyzer and polarizer prisms optical activity on the spectra shown in Figs. 8-12, we found a net effect in ε of the order of 1% as estimated by Aspnes [23]. We share the conclusion of Ref. 23 that sample preparation is more important than correction of prisms optical activity.

6. Conclusions

We have designed and constructed a full operative spectroscopic ellipsometer. The accurate control of the polarizer angle and of the analyzer angular frequency, allow us to measure the spectroscopic dielectric function of several semiconductors with high precision and with a high signal-to-noise ratio.

∗   CONACyT fellow

∗∗ Corresponding author: Phone: +52-444-825-0183; fax: +52-444-825-01-98; e-mail: lflm@cactus.iico.uaslp.mx

1. P. Yu and M. Cardona, *Fundametals of Semiconductors. Physics and Material Properties* (Springer-Verlag, Berlin, 1996) p. 237.

2. D.E. Aspnes and A.A. Studna, *Phys. Rev. B* **27**(2) (1983) 985.

3. M. Muñoz *et al.*, *J. Appl. Phys.* **87**(4) (2000) 1780.

4. A.B. Djurišić, Y. Chan, and E. Hebert Li,*Materials Science and Engineering R* **38**(6) (2002) 237.

5. S. Adachi, *J. Appl. Phys.* **66**(12) (1989) 6030.

6. D.E. Aspnes, *SPIE proc.* **946** (1988) 84.

7. D.E. Aspnes, S.M. Kelso, R.A. Logan, and R. Bhat, *J. Appl. Phys.* **60** (1986) 754.

8. Pickering, R.T. Carline, T. Emeny, N.S. Garawal, and L.K. Howard, *Appl. Phys. Lett.* **60**(19) (1992) 2412.

9. J.H. Bahng *et al.*, *Solid State Communications* **120** (2001) 343.

10. M. Garriga *et al.*, *Phys. Rev. B* **36** (1987) 3254.

11. R.P. Vasquez, R.T. Kuoda, and A. Madhukar, *J. Appl. Phys.* **61**(8) (1987) 2973.

12. U. Schmid, N.E. Christensen, M. Cardona, F. Lukeš, and K. Ploog, *Phys. Rev. B* **45**(7) (1992) 3546.

13. R.M. A Azzam and N.M. Bashara, *Ellipsometry and Polarized Light* (North Holland, Amsterdam, 1987) p. vi.

14. D.E. Aspnes and A.A. Stunda, *Appl. Optics* **14**(1) (1975) 220.

15. P.S. Hauge and F.H. Dill, *IBM J. Res. Devel.* **17** (1973) 472.

16. S.N. Jasperson and S.E. Schnatterly, *Rev. Sci. Instrum.* **40** (1969) 761.

17. B.D. Cahan and R.F. Spanier, *Surface Science* **16** (1969) 166.

18. H. Kuzmani, *Solid State Spectroscopy. An Introduction* (Springer, Germany, 1998) p. 101.

19. D. Kliger, J. Lewis, and, C. Randall, *Polarized Light in Optics and Spectroscopy* (Academic Press, USA, 1990) 92.

20. See Ref. 13, p. 257.

21. H. Tompkins, *A Users Guide to Ellipsometry* (Academic Press, USA, 1993) 17.

22. Definition of ρ after Drude, the inverse also can be used by regarding consistency. R.H. Muller *Surface Science* **16** (1969) 14.

23. D.E. Aspnes, *J. Opt. Soc. Am.* **64**(6) (1974) 812.

24. L.F. Lastras, R.E. Balderas, and A. Lastras, *Rev. Sci. Instrum.* **64** (1993) 2147.

25. SGS-Thomson Microelectronics L297/A/D Stepper motor controllers.

26. National Semiconductor *Linear Data-book* (1999). URL:http://cache.national.com/ds/LM/LM628.pdf

27. TEXAS INSTRUMENTS INCORPORATED. Semiconductor Group, *The TTL Data-book*.

28. L.F. Lastras, *Master Degree Thesis* Unpublished.

29. O. S. Heavens, *Optical Properties of Thin Solid Films* (Dover, USA, 1991) 63.

30. D.E. Aspnes, B. Schwartz, A.A. Studna, L. Derick, and L.A. Koszi, *J. Appl. Phys.* **48**(8) (1977) 3510.

31. Elements and III-V Compounds, edited by O. Madelung, M. Schultz and H. Weiss, Landolt-Börnstein, New Series, Vol. III/17a (Springer-Verlag Berlin 1982).

32. L. Viña, C. Umbach, M. Cardona, and L. Vodopyanov, *Phys. Rev. B* **29** (1984) 6752.

33. H. Arwin and D.E. Aspnes *J. Vac. Technol. A* **2**(3) (1984) 1316.

34. P. Lautenschlager, M. Garriga, S. Logothedis, and M. Cardona *Phys. Rev. B* **35**(17) (1987) 9174.